

# Instability of Gravity Driven Flow of Liquid Crystal Films

SEAN P. NAUGHTON, NAMRATA K. PATEL\*, IVANA SERIC  
ADVISORS: L. KONDIC, T-S. LIN, L. J. CUMMINGS

Department of Mathematical Sciences  
New Jersey Institute of Technology, Newark, NJ 07102

April 18, 2012

## Abstract

This paper discusses modeling of spreading nematic liquid crystal films. We concentrate on gravity driven spreading and consider various instabilities which occur during the spreading. We find that nematic character of the spreading film leads to stronger instabilities of the film fronts, and that it also leads to surface instabilities. We also present results of physical experiments involving spreading nematic films and find good agreement with the theoretical and computational predictions.

## 1 Background

As the name suggests, ‘liquid crystals’ exist in an intermediate state between a liquid and a solid. The term may be misleading however, they are not a crystal, and they need not be a liquid. Liquid crystals exist all around us in everyday life - in plastics, crude oil, lipstick, and many other places [2]. Their most widely known industrial application is in Liquid crystal displays (LCDs), which are of enormous technological importance. These, and other commercially-important applications of liquid crystals, provide a drive for a greater understanding of their properties.

---

\*Current Address: Department of Engineering Sciences and Applied Mathematics, Northwestern University, Evanston, IL 60208, USA.

Liquid crystals exist in a variety of mesophases; we focus only on the nematic phase. Nematic liquid crystals (NLCs) consist of rod-like molecules, which prefer to align locally. This local alignment gives rise to the ‘crystal’-like structure; however there is no long-range ordering of the molecular direction (this aspect makes liquid crystals similar to liquids). A more detailed but accessible introduction to liquid crystals of all types can be found in a recent review article [2].

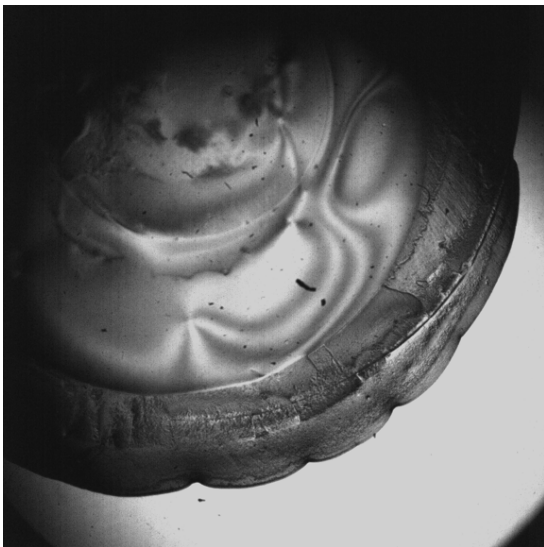


Figure 1: Instabilities observed during spreading of liquid crystal drops on horizontal substrate, from [1].

are carried out on spreading NLC droplets, and it is found that the droplets can either spread stably, or destabilize. Stable spreading means that a droplet has a smooth perimeter; while unstable infers various irregularities along the perimeter and on the free surface. Figure 1 illustrates some of these instabilities [1]. Different phenomena are observed as the relative humidity, temperature, and droplet size are varied, as discussed in the literature [7].

This spreading NLC droplet scenario has been considered from a theoretical viewpoint [5, 6], but little theoretical work has been done on the relatively simple problem of gravity driven spreading of NLC film down an inclined plane. The behavior of a Newtonian fluid flowing in this setting is well understood [8]. In this paper we investigate the behavior of a thin film of NLC flowing down an incline instead; in particular, how the behavior differs from the Newtonian case. We will discuss the dynamics of such NLC films using linear stability analysis (LSA), two and three dimensional numerical simulations of a theoretical

The preferred orientation of the NLC molecules may be described by the director field  $\mathbf{n}$ , a (unit) vector function of position and time, which we will describe in more detail later. External forces tend to distort this preferred molecular configuration causing the NLCs to undergo elastic deformations such as splaying, twisting, or bending [3, 4].

A body of existing research in the field revolves around instabilities forming in the spreading of liquid crystals, and their possible interaction with ‘defects’ [5, 6, 7]. The term ‘defect’ refers to discontinuities in the director field of the NLCs’ molecules. More details about defects can be found in the literature (see for example the classic text by De Gennes & Prost[3]). The instability involves the shape of the perimeter of a droplet which is laid on a surface (either horizontal or inclined), or the shape of the droplet itself. In [7], a series of experiments

model, and physical experiments. We first introduce the evolution equation derived within long wave theory in §2. In §3 we consider the two dimensional (2D) physical problem and carry out linear stability analysis and simulations in this simplified geometry. Then, in §4, the 3D simulations are discussed with an emphasis on extracting the growth rates of the unstable patterns that form, and on comparing them to the results of the LSA. Finally, in §5 we discuss our experimental results and compare the findings to the theoretical and computational results.

## 2 Evolution equation

A simplified model describing the flow of a thin film of NLCs using long wave theory and assuming that the unperturbed flow is 2D can be found in [5] and a basic introduction to long wave theory in [8, 10]. The model [5] describes the evolution of the film height  $h(x, y, z, t)$  of NLCs on a rigid substrate driven by a constant flux at the far-field. This model will be a starting point for our work.

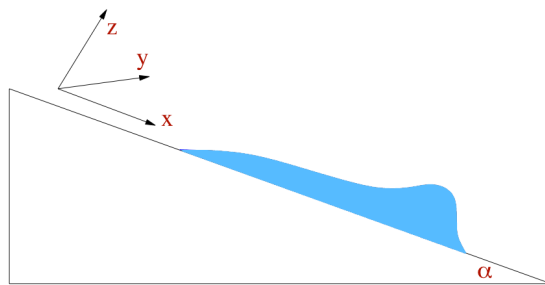


Figure 2: (a) Schematic diagram of NLCs flowing down a substrate with an inclination angle  $\alpha$ .

To start with, we define our coordinate system  $(x, y, z)$  such that  $(x, y)$  are the in-plane coordinates defining the plane of spreading, with  $x$  defining the direction of greatest slope; while  $z$  is the out-of-plane coordinate (see Figure 2). Since the nematic director field is a unit vector, in general it may be written as  $\mathbf{n} = (\sin \theta \cos \phi, \sin \theta \sin \phi, \cos \theta)$ , a vector that represents the local preferred orientation of the nematic molecules. The angle  $\theta(x, y, z, t)$  is measured with respect to the  $(x, y)$  plane, with  $\theta = 0$  being normal to this plane. The azimuthal angle  $\phi(x, y, z, t)$  specifies the director orientation in the  $(x, y)$  plane; for simplicity here we assume as in [11] that  $\phi = 0$ , so that the director field lies in a plane, and simplifies to  $\mathbf{n} = (\sin \theta, 0, \cos \theta)$ . We still allow for a fully three-dimensional fluid velocity; within lubrication approach this three-dimensional velocity is reduced to two dimensions. The director orientation can be influenced by many factors including external electromagnetic fields, and the surface with which it is in contact [3]. The preferred orientation at the interface of the liquid crystal and its surrounding (i.e. the substrate or the air) is referred to as anchoring. In the case of strong anchoring,

the director takes a fixed angle at the surface. In general, these fixed directions are not the same at the flat substrate and at the free surface. One may define a parameter  $\Delta\Theta$ , representative of the difference between the preferred value of the director angle  $\theta$  at the free surface, and that at the substrate. When  $\Delta\Theta \neq 0$ , the strong anchoring model becomes ill-posed at the contact line, where the strong anchoring dictates that the director must take upon two distinct orientations at a single point (one parallel to the substrate and one orthogonal to the film of NLCs). This contradiction was addressed by Cummings et al. [6] in a weak anchoring model. The nondimensional evolution equation derived in [6] for a film of height  $h(x, y, z, t)$  spreading on a horizontal substrate is given by

$$h_t + \nabla \cdot [h^3(\mathcal{C}\nabla\nabla^2h - \mathcal{B}\nabla h) + \mathcal{N}(m^2 - h m m')\nabla h] = 0, \quad (1)$$

$$m(h) = \frac{h^{3/2}}{\beta^{3/2} + h^{3/2}}. \quad (2)$$

(The scales and nondimensional parameters associated with the terms in (1) are summarized below where “\*” denotes dimensional parameters.) The fourth-order term proportional to  $\mathcal{C}$  is due to the capillary effects involving surface tension which has a flattening effect at the free surface [8]. The term proportional to  $\mathcal{B}$  is due to hydrostatic pressure, and the remaining terms are due to the liquid crystalline nature of the spreading fluid. Here  $\beta$  is introduced as a parameter to govern the anchoring is weak or strong. In the weak anchoring model, a surface energy is assigned to the boundary with a finite anchoring strength, allowing the director to bend through successively smaller angles as the film height  $h$  decreases, with the bending angle approaching zero as the film thickness  $h \rightarrow 0$  [6]. This behavior is modeled by introducing the monotone function of film height,  $m(h)$ , describing weak anchoring when  $h \ll \beta$  and strong anchoring when the inequality is reversed, including the special case of  $\beta = 0$  in which the nematic term takes the form of negative diffusion, as discussed in [6]. Dimensionally, the anchoring condition is relaxed over the length scale  $\beta^* = \beta H^*$ , where  $H^*$  is the characteristic film height [6]. Also, the parameter  $\delta = H^*/L^* \ll 1$  is introduced (the ratio of the characteristic film height  $H^*$  and the characteristic length  $L^*$  of the liquid crystal drop). The long wave approximation [12] was adopted in deriving the above flow equation. Furthermore, it was assumed that the substrate was prewetted with a precursor layer of thickness  $b \ll h$  extending to  $x = \infty$  (see also [5]). The scales used are defined as follows

$$(x^*, y^*, z^*) = L^*(x, y, \delta z), \quad t^* = \frac{L^*}{3U^*}t, \quad h^* = H^*h, \quad (3)$$

$$\mathcal{C} = \frac{\delta^3 \gamma^*}{\mu^* U^*}, \quad \mathcal{B} = \frac{\delta^3 \rho^* g^* L^{*2}}{\mu^* U^*} \sin \alpha, \quad \mathcal{N} = \frac{5(\Delta\Theta)^2 K^*}{2\mu^* U^* L^*} \quad (4)$$

(the equation (2) assumes the inclination angle of the substrate  $\alpha = 0$ ). Here,  $U^*$  is the characteristic flow velocity in the  $x^*$ -direction. The inverse Capillary number  $\mathcal{C}$  is defined as the ratio of surface tension to viscous forces, the Bond number  $\mathcal{B}$  is defined as the ratio of density to viscous forces, and the inverse Ericksen number  $\mathcal{N}$  is defined as the ratio of the elastic forces to viscous forces. In (4), the density of the NLCs is denoted as

$\rho^*$ ,  $K^*$  is the representative elastic constant,  $\gamma^*$  is the surface tension,  $\mu^* = \alpha_4^*/2$  is the (positive) representative viscosity scale with  $\alpha_4$  as a constant in the equation that governs the viscosity (see [6] for further details), and  $g^*$  is gravity.

For the inclined case, the downhill component of gravity is added to (1) resulting in the following formulation [8]

$$h_t + \nabla \cdot [h^3(\mathcal{C}\nabla\nabla^2h - \mathcal{B}\nabla h) + \mathcal{N}(m^2 - hmm')\nabla h] + \mathcal{U}(h^3)_x = 0. \quad (5)$$

Here,  $\mathcal{U} = \delta^3\rho^*g^*L^{*2}/(\mu^*U^*)\cos\alpha$ , and this additional term describes the tangential component of gravity,  $g^*$ , acting in the downhill direction.

### 3 Two dimensional flow

The evolution equation is quite complex and hence difficult to analyze. Below, we present several scenarios where perturbations and approximations are applied to predict the overall behavior of the system, and we derive conditions necessary for developing instabilities. First, we analyze the linear stability of a uniform film and the traveling wave for the 2D problem, where it is assumed that the flow is independent of the transverse ( $y$ ) coordinate. Afterwards, we use linear stability analysis (LSA) to predict the stability of the 2D traveling wave with respect to transverse perturbations.

#### 3.1 Linear stability analysis of a uniform film

Let us first consider the simple case of perturbations to a flat film of constant thickness  $h_o$  and assume that  $h$  is independent of  $y$ . Then (5) reduces to

$$h_t + \partial_x[h^3(\mathcal{C}h_{xxx} - \mathcal{B}h_x) + \mathcal{N}(m^2 - hmm')h_x] + \mathcal{U}(h^3)_x = 0. \quad (6)$$

Perturbing the profile by a small amplitude of order  $\epsilon$  where  $0 < \epsilon \ll 1$ , we have

$$h(x, t) = h_o + \epsilon h_1(x, t) + O(\epsilon^2), \quad (7)$$

and substituting (7) into (6), we find that the  $O(\epsilon)$  equation is

$$h_{1t} + \mathcal{C}h_o^3h_{1xxxx} - (\mathcal{B} - \mathcal{N}M(h_o))h_o^3h_{1xx} + 3\mathcal{U}h_o^2h_{1x} = 0, \quad (8)$$

$$M(h_o) = \frac{h_o^{3/2} - \beta^{3/2}/2}{(h_o^{3/2} + \beta^{3/2})^3}. \quad (9)$$

The dispersion relation can be obtained by assuming solutions of the form  $h_1 \propto e^{\sigma t + ikx}$  and substituting into (8)

$$\sigma(k) = -\mathcal{C}h_o^3k^4 + (\mathcal{B} - \mathcal{N}M(h_o))h_o^3k^2 - i3\mathcal{U}h_o^2k. \quad (10)$$

Here,  $k$  is the wavenumber, and  $\sigma$  is the complex-valued growth rate. The imaginary part of the growth rate is responsible for translation and does not affect the stability. Surface tension is responsible for stabilizing the system, hence a decaying curve for  $Re(\sigma)$  vs.  $k$  is obtained for perturbations characterized by large wavenumbers  $k > k_c = \sqrt{(\mathcal{N}M(h_o) - \mathcal{B})/\mathcal{C}}$  (see Figure 3). When  $\mathcal{N}M(h_o) > \mathcal{B}$ ,  $Re(\sigma) > 0$  for wavenumbers  $0 < k < k_c$  as shown in Figure 3, hence solutions are unstable leading to the development of instabilities. The fastest growing wavenumber,  $k_m$ , occurs at the maximum of  $Re \sigma$ , and the corresponding growth-rate,  $\sigma_m$  is given by (for  $\mathcal{N}M(h_o) - \mathcal{B} > 0$ )

$$k_m = \sqrt{\frac{\mathcal{N}M(h_o) - \mathcal{B}}{2\mathcal{C}}}, \quad (11)$$

$$\sigma_m = \frac{(\mathcal{N}M(h_o) - \mathcal{B})^2}{4\mathcal{C}} h_o^3. \quad (12)$$

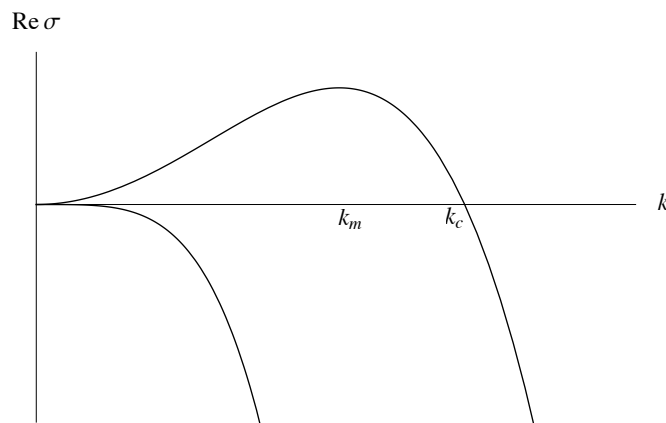


Figure 3: The growth rate as a function of the wavenumber plotted for the two cases  $\mathcal{N}M(h_o) < \mathcal{B}$  and  $\mathcal{N}M(h_o) > \mathcal{B}$ . Note that instabilities occur only for the latter case when  $0 < k < k_c$ .

### 3.2 Traveling wave solutions for the two dimensional flow

Proceeding to the traveling wave problem for the 2D evolution equation (6), we now consider a semi-infinite layer of nematic film flowing down an incline. We use the following boundary conditions

$$\begin{aligned} h &\rightarrow b, & h_x &\rightarrow 0, & \text{as } x &\rightarrow \infty, \\ h &\rightarrow 1, & h_x &\rightarrow 0, & \text{as } x &\rightarrow -\infty. \end{aligned} \quad (13)$$

We again seek a leading order solution  $h_o(x)$  independent of  $y$ . The fluid is of thickness  $h_o = 1$  behind the front and  $h_o = b$  ( $b \ll 1$  is the precursor film thickness) far ahead of the front.

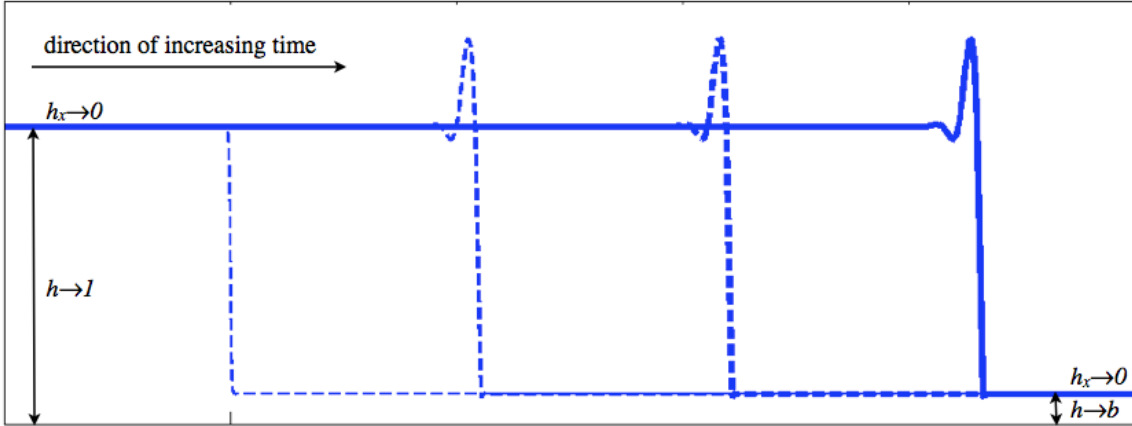


Figure 4: Traveling wave propagating from left to right shown at few different times. Here  $\mathcal{N} = 0$ .

Expecting traveling wave solutions for the fluid front, we analyze (6) in a moving reference frame by introducing the change of variable  $\xi = x - Vt$ , where  $V$  is the velocity of the wave. Substituting  $h_o(\xi) = h(x, t)$  into (6) and integrating once with respect to  $\xi$ , we obtain

$$-Vh_o + \mathcal{C}h_o^3 h_{o\xi\xi\xi} - \mathcal{B}h_o^3 h_{o\xi} + \mathcal{N}M(h_o)h_{o\xi} + \mathcal{U}h_o^3 = d, \quad (14)$$

where  $d$  is the constant of integration. Applying the boundary conditions given in (13), we find that  $d = -b(1 + b)$  and  $V = \mathcal{U}(1 + b + b^2)$ . In the case when  $\mathcal{N} = 0$ , (14) collapses to the Newtonian case and agrees with the results discussed by Kondic [8] and Bertozzi and Brenner [9]. Also since the integration constant and wave speed are independent of the inverse Erickson number  $\mathcal{N}$ , these quantities here are identical as those found in the Newtonian case [8] even for  $\mathcal{N} \neq 0$ . For illustration, Fig. 4 shows the traveling wave profiles at few times obtained by solving numerically equation (8) with the boundary conditions specified by (13).

### 3.3 Two Dimensional Simulations

The motivation for these simulations is to explore behavior of the semi-infinite fluid film flowing down an inclined plane, assuming that the flow remains  $y$ -independent, see (6). Numerical solutions are obtained using the method described in some detail in [8]. The method is based on second-order accurate finite difference discretization in space with implicit Crank-Nicolson discretization in time. The boundary conditions are as follows

$$h(0, t) = 1, \quad h_x(0, t) = 0, \quad h(L, t) = b, \quad h_x(L, t) = 0. \quad (15)$$

The precursor film thickness is set to  $b = 0.1$ . Our initial condition is a smoothed step-function, a hyperbolic tangent smoothly transitioning the film from thickness  $h = 1$  to  $h = b$  as in [13]. In our simulations, we use  $\beta = 1$  (weak anchoring) and vary  $\mathcal{N}$  (the inverse Erickson number) to explore its influence on the flow behavior. We note that the exact value of  $\mathcal{N}$  is not known and it depends on a number of factors including viscous and elastic forces; the estimates given in [6] suggest that values in the range  $O(1) - O(10)$  are reasonable.

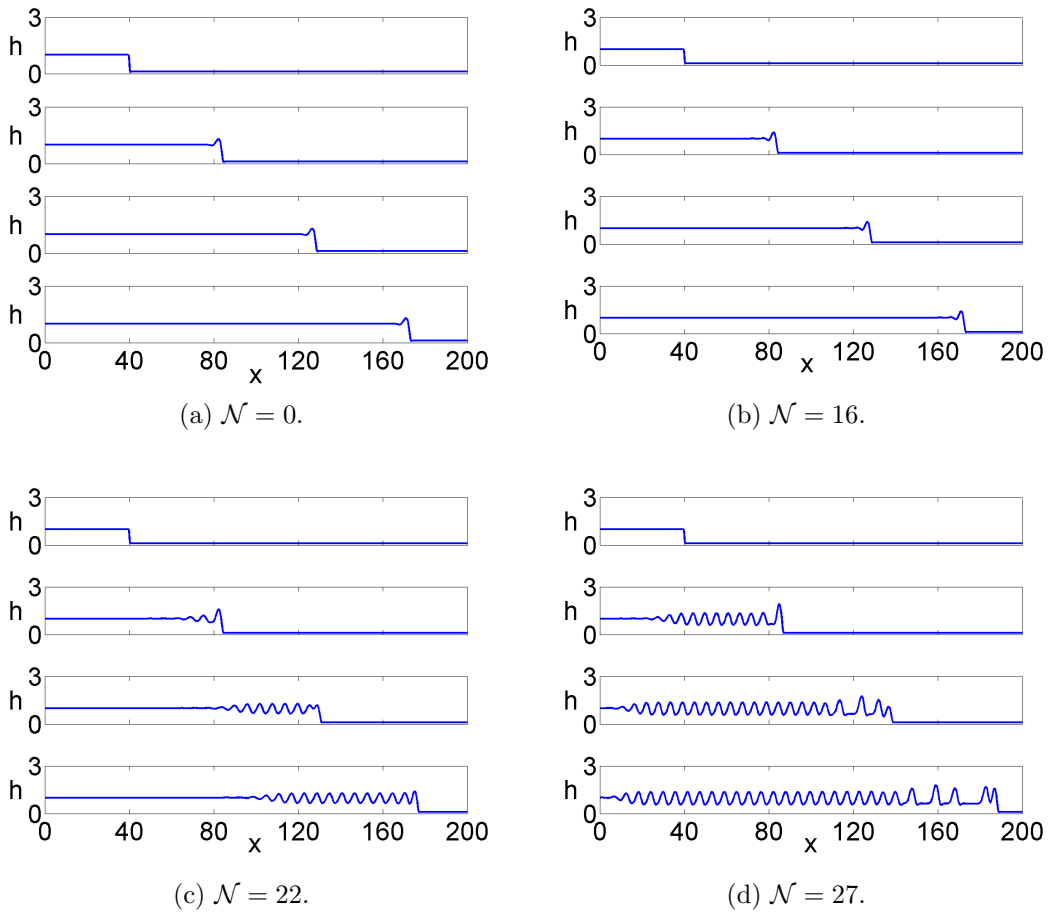


Figure 5: Simulations for the vertical plane flow ( $\alpha = \pi/2$ ). (a) Newtonian case shown from top to bottom at times  $t = 0, 40, 80, 120$ . Stable fluid flow (b), convective instability (c) and absolute instability (d) shown at the same times as in (a).

We start by considering the flow down a vertical plane,  $\alpha = \pi/2$ . Figure 5 shows the results where the parameter  $\mathcal{N}$  is progressively increased. For small values of  $\mathcal{N}$ , including



$\mathcal{N} = 0$  (Newtonian fluid) we find a stable traveling wave solution, characterized by the dominant capillary ridge, followed by a secondary, strongly damped oscillation. (Note that stability within this 2D framework is only with respect to  $x$ -dependent perturbations, not  $y$ -dependent.) As an example, Figure 5b shows the wave profile for  $\mathcal{N} = 16$  at different times. For  $t > 0$ , we observe a traveling wave solution with a constant velocity which agrees with the result obtained from LSA ( $V = \mathcal{U}(1 + b + b^2)$ ). For larger values of  $\mathcal{N}$ , we find a convective instability regime, characterized by sinusoidal waves followed by a constant state. Figure 5c illustrates the corresponding wave profile for  $\mathcal{N} = 22$ . The capillary ridge is still dominant; however, since the waves that form behind the front propagate faster than the front, when the first wave reaches the front, it interacts and merges with it. As the front moves forward, its height decreases until the next wave arrives; therefore, the velocity of the front is not constant anymore. For even larger values of  $\mathcal{N}$ , we observe an absolute instability regime, where the instability propagates upstream. Figure 5d illustrates this regime. For early times we still observe a flat film, which disappears after a sufficiently long time. We note two kinds of waves: sinusoidal waves and solitary type waves, similarly as in [13] where a flow of Newtonian fluid, but under inverted gravity conditions ( $\alpha > \pi/2$ ) was considered. Critical values for  $\mathcal{N}$  where a transition occurs from stability to convective instability ( $\mathcal{N}_{c1}$ ) and from convective to absolute instability ( $\mathcal{N}_{c2}$ ) were found from numerical simulations by trail and error and are given in Table 1. An additional insight regarding the transition between the different regimes can be obtained using LSA, which we discuss next.

### 3.3.1 Finding critical values of $\mathcal{N}$ from LSA

To find the value of  $\mathcal{N}$  where the transition occurs from stability to convective instability ( $\mathcal{N}_{c1}$ ) and from convective to absolute instability ( $\mathcal{N}_{c2}$ ), we will study the speed of the boundary of the expanding wave packet. Let us consider the governing equation (5) again, and also consider the dispersion relation given by (10) with  $h_o = 1$ . Rewriting  $\sigma = \sigma_r + i\sigma_i$  where  $\sigma_r$  and  $\sigma_i$  are respectively the real and imaginary parts of the growth rate, we have

$$\sigma_r = -\mathcal{C}k^4 + (\mathcal{B} - \mathcal{N}M(1))k^2 \quad \sigma_i = -3\mathcal{U}k. \quad (16)$$

Furthermore, following the same approach as in [13], we find that the speed of the left and right boundary of the wave packet is given by

$$\left(\frac{x}{t}\right)_{\pm} = 3\mathcal{U} \pm 1.62 \left( -\mathcal{B} + \mathcal{N} \frac{1 - \beta^{\frac{3}{2}}}{(\beta^{\frac{3}{2}} + 1)^3} \right)^{\frac{3}{2}}. \quad (17)$$

For  $\alpha = \pi/2$ , we have  $\mathcal{C} = 1$ ,  $\mathcal{B} = 0$ ,  $\mathcal{U} = 1$ ,  $\beta = 1$ , and  $(x/t)_{\pm} = 3 \pm 1.62(\mathcal{N}/16)^{\frac{3}{2}}$ . We see that the speed of the right moving boundary  $(x/t)_{+}$  is always positive and greater than the speed of the leading capillary ridge, which is given by the speed of the traveling wave solution in Section 3.2 as  $V = \mathcal{U}(1 + b + b^2)$ . This explains why waves catch up and

merge with the front. The left moving boundary will determine which kind of wave profile will appear. If the speed of the left boundary,  $(x/t)_-$ , is positive, then that boundary will move to the right. However, if it is slower than the front ( $V = 1 + b + b^2$ ), the region with sine-like waves will still grow, but there will always be a constant state region. Therefore, we will have convective instability for  $0 < 3 - 1.62(\mathcal{N}/16)^{\frac{3}{2}} < 1.11$ . Solving for  $\mathcal{N}$  yields  $17.79 < \mathcal{N} < 24.13$ . Comparison with the numerical results is given in Table 1. We can see that the results agree within 5%. Similar results are obtained for the flow down an inclined plane, with  $\alpha = \pi/4$ .

	$\alpha = \pi/2$		$\alpha = \pi/4$	
	Num	LSA	Num	LSA
$\mathcal{N}_{c1}$	18.6	17.79	25.43	25.44
$\mathcal{N}_{c2}$	24.4	24.13	30.6	30.46

Table 1: Critical values for  $\mathcal{N}$  where a transition occurs from stability to convective instability ( $\mathcal{N}_{c1}$ ) and from convective to absolute instability ( $\mathcal{N}_{c2}$ ). Values are given for vertical ( $\alpha = \pi/2$ ) and inclined ( $\alpha = \pi/4$ ) planes as retrieved from the numerical simulations and LSA for equation (6).

## 4 Three Dimensional Flow

### 4.1 Linear Stability Analysis of the Traveling Wave Solution

For Newtonian fluids, it is known that a film flowing down an incline is unstable with respect to transverse perturbations [8], leading to the formation of finger-like patterns. To analyze this problem for a NLC film, we perform LSA of the 3D model (5) by perturbing the traveling-wave profile in the direction transverse to the flow. We consider again the constant flux driven flow of a semi-infinite film, but now allow for transverse perturbations.

To analyze the stability, we apply a small perturbation at the leading order equation given by (14) and analyze the flow stability. Considering a semi-infinite domain, we write the solution in the form

$$h(x, y, t) = h_o(\xi) + \epsilon\phi(\xi)e^{\sigma t + iky} + O(\epsilon^2), \quad (18)$$

and upon substituting into (5), we find the  $O(\epsilon)$  equation

$$\begin{aligned}
-\sigma\phi &= -V\phi_\xi + \mathcal{C} \left[ k^4 h_o^3 \phi - k^2 \left( (h_o^3 \phi_\xi)_\xi + h_o^3 \phi_{\xi\xi} \right) + (h_o^3 \phi_{\xi\xi\xi} + 3h_o^2 h_{o\xi\xi\xi} \phi)_\xi \right] \\
&+ \mathcal{B} \left( k^2 h_o^3 \phi - (h_o^3 \phi)_{\xi\xi} \right) + \mathcal{N} \left( -k^2 M\phi + (M\phi)_{\xi\xi} \right) \\
&+ 3\mathcal{U}(h_o^2 \phi)_\xi .
\end{aligned} \tag{19}$$

For brevity, we use  $M = M(h_o(\xi))$  here (recall  $M$  was defined in (9)). Since (19) contains only even powers of  $k$ , the solution should also depend only on even powers. Hence, in the limit of a small wavenumber  $k$ , corresponding to long wavelength perturbations of wavelength  $\lambda = 2\pi/k$ , we apply the following asymptotic expansion

$$\phi = \phi_o + k^2 \phi_1 + O(k^4), \quad \sigma = \sigma_o + k^2 \sigma_1 + O(k^4). \tag{20}$$

Substituting (20) into (19), the leading order equation is

$$\begin{aligned}
-\sigma_o \phi_o &= \left[ -V\phi_o + \mathcal{C}(h_o^3 \phi_{o\xi\xi\xi} + 3h_o^2 h_{o\xi\xi\xi} \phi_o) - \mathcal{B}(h_o^3 \phi_{o\xi} + 3h_o^2 h_{o\xi} \phi_o) \right. \\
&\left. + \mathcal{N}(M h_{o\xi\xi} + M h_o h_{o\xi}^2) + 3\mathcal{U} h_o^2 \phi_o \right]_\xi .
\end{aligned} \tag{21}$$

In [8], the position of the contact line modified by the perturbation in (18) was considered and the boundary conditions were accordingly linearized and it was concluded that  $\phi_o(\xi) = h_{o\xi}(\xi)$ . Substituting this expression into (21), we find

$$-\sigma_o h_{o\xi} = \left[ -V h_o + \mathcal{C} h_o^3 h_{o\xi\xi\xi} - \mathcal{B} h_o^3 h_{o\xi} + \mathcal{N} M h_{o\xi} + \mathcal{U} h_o^3 \right]_{\xi\xi}. \tag{22}$$

Since the right hand side is the leading order equation we conclude that  $\sigma_o = 0$ . The  $O(k^2)$  is given by

$$\begin{aligned}
-\sigma_1 h_{o\xi} &= -V\phi_{1\xi} + \mathcal{C} \left( -h_o^3 h_{o\xi\xi\xi} + (-h_o^3 h_{o\xi\xi} + h_o^3 \phi_{1\xi\xi\xi} + 3h_o^2 h_{o\xi\xi\xi} \phi_1)_\xi \right) \\
&+ \mathcal{B} \left( h_o^3 h_{o\xi} - (h_o^3 \phi_1)_{\xi\xi} \right) + \mathcal{N} \left( -M h_{o\xi} + (M\phi_1)_{\xi\xi} \right) + 3\mathcal{U}(h_o^2 \phi_1)_\xi .
\end{aligned} \tag{23}$$

Integrating (23) and applying the boundary conditions given by (15), we obtain

$$\sigma_1(k) = -\frac{1}{1-b} \int_{-\infty}^{\infty} (\mathcal{C} h_o^3 h_{o\xi\xi\xi} - \mathcal{B} h_o^3 h_{o\xi} + \mathcal{N} M h_{o\xi}) d\xi. \tag{24}$$

Using (14) to simplify the integrand, (24) becomes

$$\sigma_1(k) = \frac{1}{1-b} \int_{-\infty}^{\infty} (b(1+b) - \mathcal{U}(1+b+b^2 - h_o^2) h_o) d\xi. \tag{25}$$

Therefore, for small  $k$  we find an approximate growth rate

$$\sigma(k) \approx \frac{k^2}{1-b} \int_{-\infty}^{\infty} (b(1+b) - \mathcal{U}(1+b+b^2 - h_o^2)h_o) d\xi. \quad (26)$$

The sign of the integral expression on the right hand side of (26) is not obvious, since the integral involves  $h_o$ , the solution of the 2D traveling wave problem. Therefore, a numerical approach is used to simulate profiles of the film height,  $h_o$ , which is then used to numerically evaluate (26). This approach is used to confirm that the behavior observed in the simulations is reflected by the theory. This is discussed in the following section.

To confirm for the reader that the result agrees with known results for Newtonian fluids, we consider the limit of a large  $\beta$ ,  $\beta \ll h_o$ . Then,  $m(h) \rightarrow 0$ , and the director field within the drop is uniform. This analysis performed throughout this section collapses the results to the Newtonian case as analyzed in [8].

## 4.2 Three Dimensional Simulations

Three dimensional simulations were carried out using the modified version of the computational code described in [14], based on an ADI (alternate direction implicit) algorithm. We use this modified code here to consider time evolution of a flow subject to a single perturbation of specified wave number. In the simulations, we vary  $N$  and the wavelength,  $\lambda$ , of the perturbation. For simplicity, we use  $\lambda = L_y$ , where  $L_y$  is the domain size in the  $y$  direction. To generate the initial condition, we perturb the traveling-wave profile from the 2D simulations discussed above, applying a cosine-like perturbation of the front position in the  $y$  direction. At the  $y$ -boundaries ( $y = 0, L_y$ ), we apply no-flow boundary conditions, by requiring  $h_y = h_{yyy} = 0$  there.

Figure 6 shows the results of simulations for a film flowing down a vertical plane in the  $+x$  direction. We see that the perturbation grows in size as time progresses, showing that we are in the unstable regime. In addition a dominant capillary ridge forms at the tip of the propagating ‘finger’, similarly as found in Newtonian case [8]. Figure 7a shows the top view of the front of the film (the intersection of the 3D profile with a plane  $z = 0.5$ ). From this 2D cross-section we find the amplitude of the perturbation as a function of time. The amplitude is taken from  $x = 0$  to the tip of the bump for each time. Figure 7b shows time evolution of the amplitude. For early times, we find exponential growth, as also illustrated in Figure 7c. For longer times, we still find that the perturbation grows, but slower than exponentially.

From the results for the amplitude, we can extract the growth rate,  $\sigma$ , of the perturbation. This is done by fitting the amplitudes to the functional form  $A(t) = A_0 e^{\sigma t}$ , where  $A(t)$  is the amplitude at the time  $t$ , and  $A_0$  is the initial amplitude, taken as  $A_0 = 0.2$ .

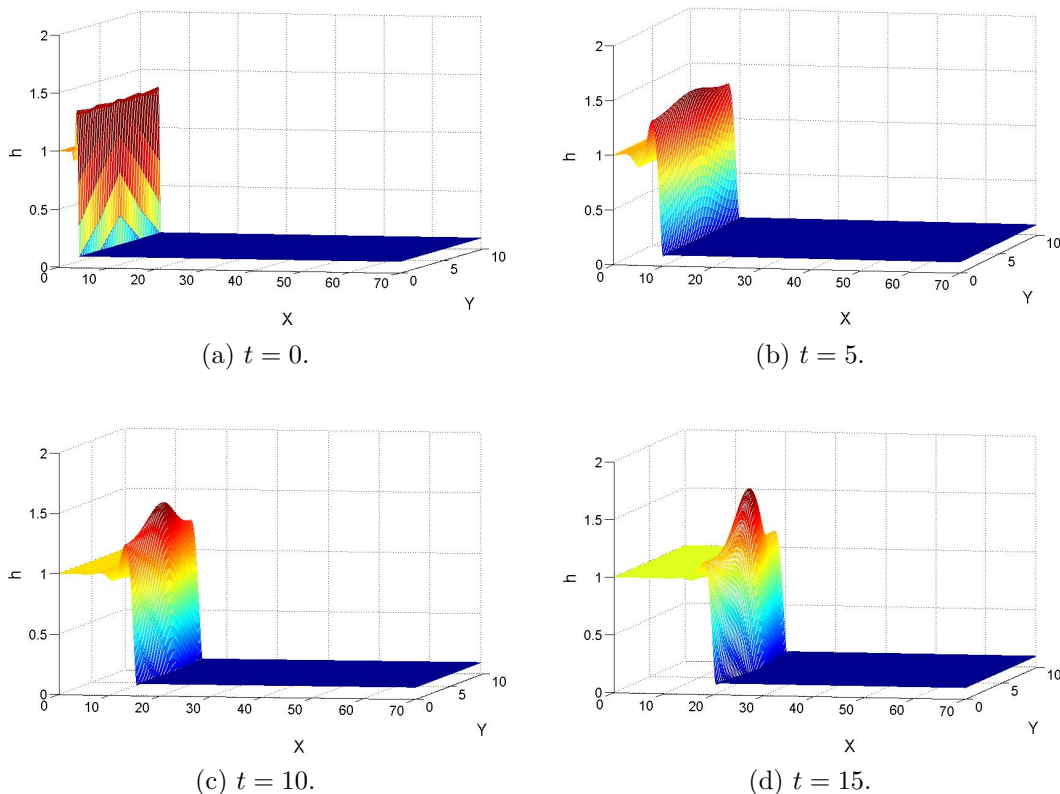
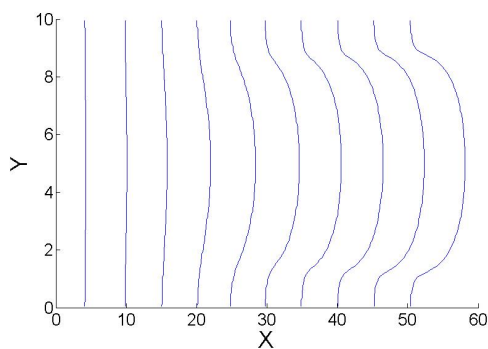


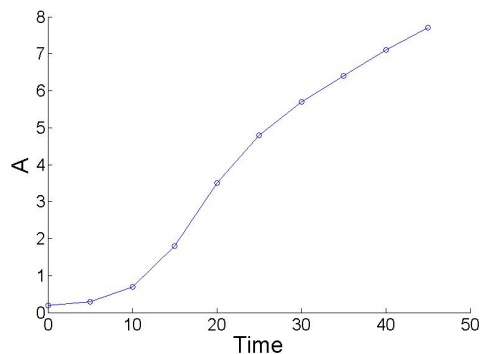
Figure 6: The results of numerical simulation of the 3D problem, showing the film thickness,  $h(x, y)$ , at times  $t = 0, 5, 10, 15$ . Here  $\mathcal{N} = 10$  and  $L_y = 10$ .

#### 4.2.1 Comparison to Linear Stability Analysis

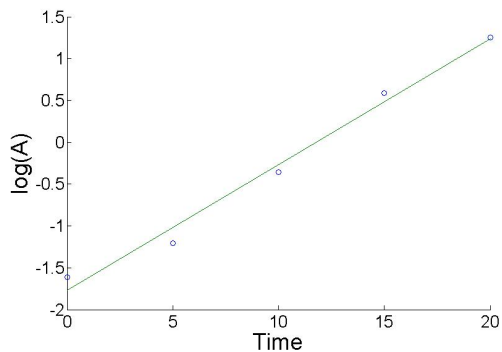
In the simulations we vary the value of  $\mathcal{N} = 0, 5, 10, 15$ , and consider  $\lambda = L_y$  in the range  $(6.5, 17)$ . As discussed below, this is the range where based on LSA we expect to find transition from stability to instability as  $\lambda$  is increased. We then extract the growth rates to discuss the degree to which these growth rates agree with the LSA results from (24) and (25). In Figure 8 we show by symbols the growth rates obtained from the 3D simulations for four different values of  $\mathcal{N}$ . In order to compare with LSA, we fit this data by a polynomial in powers of  $k^2$ , where  $k$  is the wavenumber. The motivation for this fit is to find predicted behavior for small  $k$ . We cannot simulate this region directly for very small  $k$ , since smaller  $k$  requires very large  $\lambda = L_y$ , and the simulations become demanding due to a large computational domain and correspondingly large number of grid points. Our first attempt was to fit the data from simulations with a quartic fit, but could not obtain a good fit with the data. It turns out however that a good agreement



(a) Top view of the fluid front.



(b) Amplitude of the perturbation.



(c) Amplitude of the perturbation for early times.

Figure 7: (a) The position of the film's front as a function of time measured at  $z = 0.5$ . (b) Amplitude of the perturbation obtained from the results shown in (a). (c) Zoomed in version of (b) showing the area of exponential growth using a logarithmic scale for the  $y$  axis. The line is the best fit approximation. Here,  $\mathcal{N} = 10$  and  $L_y = 10$ . For this case, we find the growth rate  $\sigma \approx 0.13$ .

can be found using an octic fit of the form

$$\sigma(k) = a_1k^2 + a_2k^4 + a_3k^6 + a_4k^8 \quad (27)$$

(lower-order polynomials do not give a good fit). The results of the fit are shown in Figure 8. This figure also compares the predictions of this fit with the LSA result (20), which holds for small  $k$ . We find the values of  $\sigma_1$  (coefficient of  $k^2$  term as in (20)) by calculating numerically the integral in (24) (with  $C = 1$ , see [6] and  $\mathcal{B} = 0$ , as appropriate for the flow down a vertical wall) for various  $\mathcal{N}$ . Table 2 lists the values of  $\sigma_1$  for several

$\mathcal{N}$	$\sigma_1$
0	1.2699
5	1.3565
10	1.4583
15	1.5754

Table 2: Values of  $\sigma_1$  for few values of  $\mathcal{N}$ .

values of  $\mathcal{N}$ . We see that increasing  $\mathcal{N}$  causes an increase in the values of  $\sigma$ , suggesting that the NLC flow is more unstable than the corresponding Newtonian fluid ( $\mathcal{N} = 0$ ). Figure 8 indicates a good agreement between the octic fit to the 3D numerical simulations, and the LSA results for small wavenumbers. For large wavenumbers, we see in Figure 8 that for larger values of  $\mathcal{N}$ , the critical wavenumber,  $k_c$ , increases, suggesting increased instability.

## 5 Experimental Results

We have also carried out simple physical experiments with NLC (4-Cyano-4-pentylbiphenyl from 2A PharmaChem ) down a vertically positioned silicon wafer. Figure 9 shows an example of our experimental results. Initially, a line of NLC (volume  $125\mu L$ ) is positioned on a horizontal wafer, which is then rotated to the vertical plane. While the fluid is spreading, we measure the time interval needed for a finger to travel a specific distance; the width of the fingers; and their distance traveled. Since the exact value of  $\mathcal{N}$  is unknown, we cannot explicitly compare experiments to specific simulation cases. Instead, we find the average wavelength (the distance between the fingers), and compare this value with the most unstable mode obtained from simulations, and we also compare the corresponding growth rates between the experiment and simulations.

In order to compare the data to the simulations and theory, we need the scales used to nondimensionalize the evolution equation:  $t^* = (L^*/U^*)t$ , and  $l^* = L^*l$ , where  $U^* = \delta^3 \rho^* g^* L^{*2} / \mu^*$  and  $L^* = \sqrt{\gamma^* / (\rho^* g^*)}$  as in [6], and  $\delta = H^* / L^*$  (we remind the reader that any parameter with the ‘\*’ superscript is dimensional). We use the numerical values for

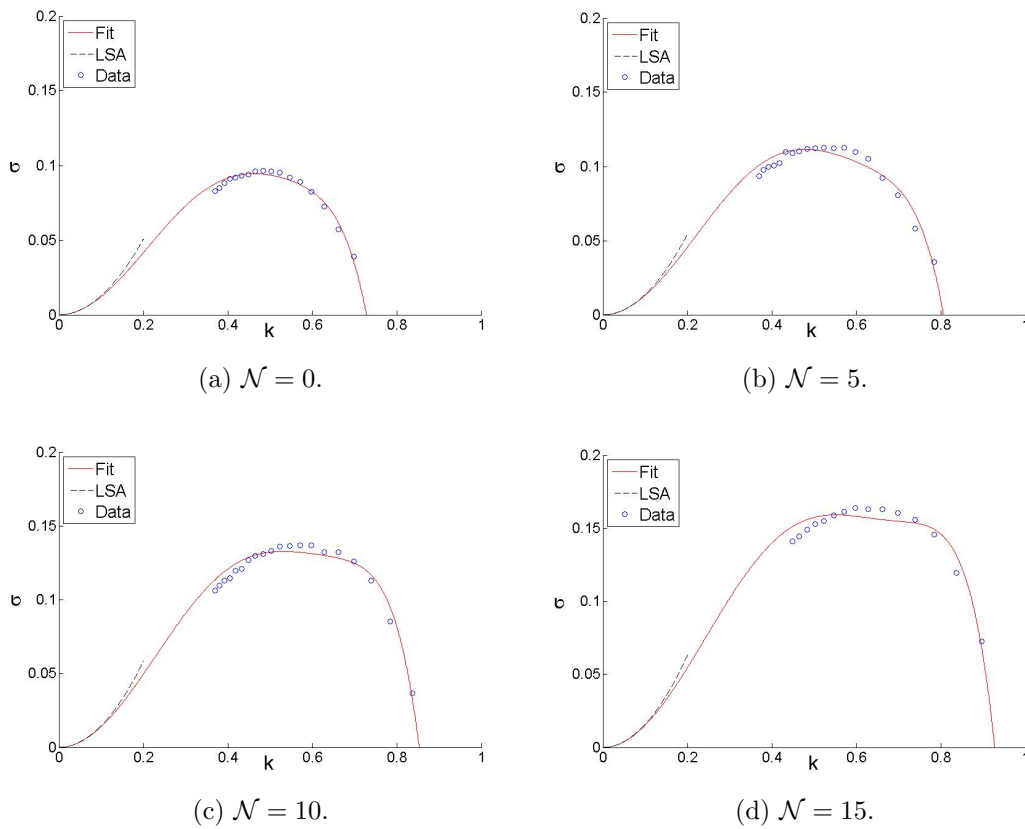


Figure 8: In each panel above, the blue dots represent the data points retrieved from the simulations, the red lines are the fits to the data as described in (27), and the black line is the quadratic form resulting from LSA in the limit of small wavenumbers,  $\sigma = \sigma_1 k^2$ , see (26).

physical parameters as specified in [6, 11]: the surface tension,  $\gamma^* \approx 3.5 \times 10^{-2}$  N/m, the density,  $\rho^* = 10^3$  kg/m<sup>3</sup>, and the viscosity,  $\mu = 4 \times 10^{-2}$  Pa s. Substituting these values gives  $L^* \approx 1.9$  mm and  $\mathcal{U} = 0.88\delta^3$ . For our experiment, the approximate value of fluid thickness is  $H^* \approx 1$ mm. Using this value we find that  $\delta \approx 0.5$ , and so  $U^* \approx 0.11$ . The average wavelength is found by dividing the total width of the domain, 7.5 cm, by the number of fingers. On average, we observe five fingers, giving the average wavelength of 1.5 cm and corresponding nondimensional wavenumber of  $k \approx 0.80$ . This value is consistent, although slightly larger than the most unstable wavenumber found in simulations, see Figure 8.

To extract the growth rates, we track the fingers' length as a function of time. We find that on average the fingers grow initially at a rate of  $\approx 1/6$  cm/s. Assuming exponential growth (as appropriate for early times), we then find the corresponding nondimensional growth rate,  $\sigma \approx 0.12$ . This value is again consistent with the growth rates found in simu-





Figure 9: Image of line of NLC flowing down silicon wafer.

lations, see Figure 8. While the present experimental setup does not allow for more precise comparison to theory, we find this order-of-magnitude agreement encouraging, showing that the theoretical model captures the main features of the instability mechanism.

## 6 Conclusion

In this work, we have compared analytical, computational, and experimental results for the flow of nematic liquid crystals down an incline in both two (2D) and three (3D) dimensions. In general, we find good agreement between the results of these different techniques.

The main result for the 2D problem is the prediction for formation of surface waves, which are due to the nematic properties of the spreading fluid. The properties of these waves, which have not been observed so far, are influenced by the parameter  $\mathcal{N}$  (inverse Ericksen number) and the inclination angle  $\alpha$ . In 3D, we find computationally that an increase of  $\mathcal{N}$  leads to increased instability, therefore predicting faster instability growth (larger growth rates) and shorter distance between emerging fingers, compared to the equivalent Newtonian fluid.

**Acknowledgments** This work is the result of an undergraduate summer research project funded by the NSF grant No. DMS-0908158 and the NJIT Provost's Undergraduate Summer Research Awards. This summer project was built upon the Capstone course in Modeling in Applied Mathematics, offered in the Spring 2011 semester, and we would like to acknowledge our colleagues in this class who have in one way or another contributed to the results presented here. These are: Paul Dupiano, Motolani Olarinre,

Juan Pineda, Priyanka Shah and Mandeep Singh. The project advisors would also like to thank P. Palffy-Muhoray from Kent State University whose experimental expertise and suggestions have been invaluable.

## References

- [1] Capstone Laboratory [http://web.njit.edu/~kondic/capstone/2011/Capstone\\_2011.html](http://web.njit.edu/~kondic/capstone/2011/Capstone_2011.html).
- [2] P. Palffy-Muhoray, The Diverse World of Liquid Crystals, *Physics Today* **60**, 54 (2007).
- [3] P.G. DeGennes and J. Prost, *The physics of liquid crystals*, (Oxford University Press, Oxford, 1993).
- [4] J. Q. Carou, Flow of a nematic liquid crystal, *Doctoral thesis at University of Strathclyde, Glasgow* (2007).
- [5] M. Ben Amar and L. J. Cummings, Fingering instabilities in driven thin nematic films, *Phys. Fluids* **13**, 5 (2001).
- [6] L. J. Cummings, T.-S. Lin, and L. Kondic, Modeling and simulations of the spreading and destabilization of nematic drops, *Phys. Fluids* **23**, 4 (2011).
- [7] C. Poulard and A. M. Cazabat, Spontaneous spreading of nematic liquid crystals, *Langmuir* **21**, 14 (2005).
- [8] L. Kondic, Instabilities in gravity driven flow of thin fluid films, *SIAM Review* **45**, 1 (2003).
- [9] A. L. Bertozzi and M. P. Brenner, Linear stability and transient growth in driven contact lines, *Phys. Fluids* **9**, 530 (1997).
- [10] D. J. Acheson, *Elementary Fluid Dynamics* (Oxford University Press, Oxford, 2003).
- [11] L. J. Cummings, Evolution of a thin film of nematic liquid crystal with anisotropic surface energy, *Eur. J. Appl Math* **15**, 6 (2004).
- [12] H. Ockendon and J.R. Ockendon. *Viscous Flow* (Cambridge University Press, New York, 1995).
- [13] T.-S. Lin and L. Kondic, Thin films flowing down inverted substrates: Two dimensional flow, *Phys. Fluids*, **22**, 052105 (2010).
- [14] T.-S. Lin and L. Kondic, Thin films flowing down inverted substrates: Three dimensional flow, *Phys. Fluids*, to appear (2012).